Non-invasive quantification of cerebrovascular pressure changes using 4D Flow MRI

Journal:	*Magnetic Resonance in Medicine*
Manuscript ID	MRM-21-21912.R1
Wiley - Manuscript type:	Full Paper
Research Type:	Image processing/Image analysis < Technical Research, Flow and perfusion < Technique Development
Research Focus:	Function < Vasculature < Cardiovascular

SCHOLARONE™
Manuscripts

Non-invasive quantification of cerebrovascular pressure changes using 4D Flow MRI

David Marlevi[a,*], Jonas Schollenberger[b], Maria Aristova[c], Edward Ferdian[d], Yue Ma[c,g], Alistair A. Young[d,e], Elazer R. Edelman[a], Susanne Schnell[c,f], C. Alberto Figueroa[b], David A. Nordsletten[b,e]

[a]Institute for Medical Engineering and Science, Massachusetts Institute of Technology, 77 Massachusetts Avenue, Cambridge, MA 02139, USA

[b]Department of Surgery and Biomedical Engineering, University of Michigan, 2800 Plymouth Rd, Ann Arbor, MI 48109, United States of America

[c]Department of Radiology, Northwestern University, 737 N. Michigan Ave, Suite 1600, Chicago, IL 60611, USA

[d]Department of Anatomy and Medical Imaging, University of Auckland, 85 Park Rd, Grafton, Auckland 1142, New Zealand

[e]School of Biomedical Engineering and Imaging Sciences, The Rayne Institute, King's College London, SE1 7EH, London, United Kingdom

[f]Department of Medical Physics, Institute of Physics, University of Greifswald, Felix-Hausdorff-Str. 6, 17489 Greifswald, Germany

[g]Department of Radiology, Shengjing Hospital of China Medical University, No.36 Sanhao St, Shenyang, 110004, China.

Word count (body of text): 5330
Figure + Table count: 8 + 2

Abstract

Purpose: Hemodynamic alterations are indicative of cerebrovascular disease. However, the narrow and tortuous cerebrovasculature complicates image-based assessment, especially when quantifying relative pressure. Here, we present a systematic evaluation of image-based cerebrovascular relative pressure mapping, investigating the accuracy of the routinely-used reduced Bernoulli (RB), the extended unsteady Bernoulli (UB), and the full-field virtual Work-Energy Relative Pressure (νWERP) method.

Methods: Patient-specific *in-silico* models were used to generate synthetic cerebrovascular 4D Flow MRI, with RB, UB, and νWERP performance quantified as a function of

*Corresponding author; *Address*: Institute for Medical Engineering and Science, Massachusetts Institute of Technology, 77 Massachusetts Avenue, Cambridge, MA 02139, USA; *E-mail*: `marlevi@mit.edu`; *Phone*: +1 (617) 253-1000

Email addresses: `marlevi@mit.edu` (David Marlevi), `scjonas@umich.edu` (Jonas Schollenberger), `maria.aristova@northwestern.edu` (Maria Aristova), `e.ferdian@auckland.ac.nz` (Edward Ferdian), `mmaayyuuee@sj-hospital.org` (Yue Ma), `alistair.young@kcl.ac.uk` (Alistair A. Young), `ere@mit.edu` (Elazer R. Edelman), `susanne.schnell@uni-greifswald.de` (Susanne Schnell), `figueroc@med.umich.edu` (C. Alberto Figueroa), `nordslet@umich.edu` (David A. Nordsletten)

spatiotemporal sampling and image noise. Cerebrovascular relative pressures were also derived in 4D Flow MRI from healthy volunteers ($n = 8$), acquired at two spatial resolutions ($dx = 1.1$ and 0.8 mm).

Results: The *in-silico* analysis indicate that accurate relative pressure estimations are inherently coupled to spatial sampling: at $dx = 1.0$ mm high errors are reported for all methods; at $dx = 0.5$ mm νWERP recovers relative pressures at a mean error of 0.02 ± 0.25 mmHg, whilst errors remain higher for RB and UB (mean error of -2.18 ± 1.91 and -2.18 ± 1.87 mmHg, respectively). The dependence on spatial sampling is also indicated *in-vivo*, albeit with higher correlative dependence between resolutions using νWERP ($k = 0.64$, $R^2 = 0.81$ for $dx = 1.1$ vs 0.8 mm) than with RB or UB ($k = 0.04$, $R^2 = 0.03$, and $k = 0.07$, $R^2 = 0.07$, respectively).

Conclusion: Image-based full-field methods such as νWERP enable cerebrovascular relative pressure mapping; however, accuracy is directly dependent on utilized spatial resolution.

Keywords: Relative pressure, Cerebrovascular, 4D Flow MRI,, Hemodynamics, Patient-specific modelling

---

1. Introduction

The onset and manifestation of cerebrovascular disease directly impacts regional hemodynamics. Alterations in pressure through sections of the cerebrovasculature have been highlighted as indicative for a number of pathological scenarios: the risk for recurrent stroke in intracranial atherosclerosis [1, 2], the development of arteriovenous malformations and cerebral aneurysms [3, 4, 5], and the manifestation of neurodegenerative disorders [6, 7]. The cerebrovasculature is, however, characterized by a complex network of narrow, tortuous, and bifurcating vessels, giving rise to intricate hemodynamic behavior [3, 8, 9]. Given the difference in vasculature and local hemodynamics, it is unclear how well traditional image-based techniques used to assess relative pressure in other cardiovascular domains translate into the cerebrovascular space. A systematic evaluation of techniques for the assessment of cerebrovascular relative pressure is thus still warranted, where a validated and accurate technique could have direct impact in a number of areas of cerebrovascular diagnostics.

In other cardiovascular domains, catheter-based measurement of intravascular pressure is standard-of-care [10, 11], although widespread use is limited due to its invasive nature [12, 13]. Doppler echocardiography is a non-invasive alternative, where relative pressure is routinely derived using a reduced-form of the Bernoulli (RB) principle [14]. Discrepancies against ground truth data [15, 16, 17, 18] have lead to higher-order Bernoulli descriptors [19, 20]. However, inherent method assumptions make the extensions of RB to complex flow

difficult to predict [15, 17]. For the cerebrovasculature, catheter-based pressure assessments do not yet have regulatory approval, and have only been performed during intervention in a strict research setting [21, 22]. Furthermore, reduced-form Bernoulli-based estimates have been derived in regional sections using transcranial Doppler [23]. The application of higher-order estimation methods has however rarely been attempted, and the complex anatomy of the cerebrovasculature might render hemodynamic patterns driven by intricate flow and flow gradients, where full-field imaging is required to accurately assess such behavior.

Time-resolved three-dimensional phase-contrast magnetic resonance imaging (4D Flow MRI) enables full-field flow quantification through multi-directional velocity encoding [24, 25]. Several studies have highlighted the applicability of 4D Flow MRI for cerebrovascular assessment [26, 27], including mapping non-diseased flow characteristics [28, 29], identifying flow features in cerebrovascular atherosclerosis [9, 18], evaluating arteriovenous malformations [30, 31, 32], or assessing hemodynamic changes in neurodegenerative disorders [33, 34]. When it comes to using 4D Flow MRI to map relative pressure in the cerebrovasculature, a few examples exist largely building on methods used in other cardiovascular domains. Vali et al. [18] used RB to estimate relative pressures over atherosclerotic intracranial vessels, still acknowledging possible estimation bias. Rivera-Rivera et al. [4] used an iterative approach to extract relative pressure fields through the dural sinus directly from the Navier-Stokes equations, and Zhang et al. [35] solved a Pressure Poisson Equation (PPE) in intracranial anuerysmal geometries with additional weighting introduced to compensate for erroneous velocity divergence. However, with methods recovering 3D relative pressure fields being dependent on accurately estimated flow gradients and flow domain definitions [36, 37], and with decreasing accuracy indicated for PPE-like methods when applied on stenotic *in-silico* flows [36, 38], the accuracy and applicability of these techniques into narrower cerebrovascular sections remains unknown. To overcome some of the limitations associated with these alternative full-field techniques, we recently presented the virtual Work-Energy Relative Pressure (νWERP) [17] method, theoretically allowing for arbitrary probing of relative pressure through complex, arbitrary flow domains. Yet, the method has never been evaluated in the cerebrovasculature. As cerebrovascular hemodynamics present with unique anatomy and flow (being in many instances distinctly different from the settings for which many of the aforementioned estimation methods were designed) such explicit examination is necessary.

The aim of this study is to systematically evaluate the ability to use 4D Flow MRI together with techniques commonly employed in other cardiovascular domains to quantify changes in cerebrovascular pressure. To represent different approaches with varying underlying assumptions and clinical usage, three methods were assessed: the routinely used reduced Bernoulli (RB) approach, the extended unsteady Bernoulli (UB) approach, and the

more recent νWERP metho - proposed to overcome limitations of other alternative full-field methods. To provide a comprehensive basis for the analysis, we utilize dedicated patient-specific *in-silico* models of the arterial cerebrovasculature, calibrated using MRI data. These models are then used to assess estimation accuracy as a function of spatiotemporal image sampling and noise. Secondly, to evaluate clinical feasibility and to assess spatial dependencies in vivo, 4D Flow MRI from a volunteer cohort was analyzed using the same three methods. In summary, the study clarifies possibilities and challenges in image-based cerebrovascular relative pressure mapping, and highlights the potential of full-field imaging in providing accurate assessment of cerebrovascular behavior.

2. Method

2.1. Review of flow-based relative pressure estimators

For any isothermal, viscous, incompressible, Newtonian fluid, the relationship between fluid velocity, $\mathbf{v}$, and pressure, p, can be described by the Navier-Stokes equations as

$$\rho \frac{\partial}{\partial t}\mathbf{v} + \rho \mathbf{v} \cdot \nabla \mathbf{v} - \mu \nabla^2 \mathbf{v} + \nabla p = 0, \tag{1}$$

$$\nabla \cdot \mathbf{v} = 0, \tag{2}$$

with ρ and μ being fluid density and dynamic viscosity, respectively. The task of any relative pressure estimator is then to isolate the pressure gradient in Eq. 1, expressing it as a function of velocity (making it applicable for flow-based medical imaging). Assuming negligible transient and viscous effects, Eq. 1 can be simplified to the reduced Bernoulli (RB) formula, e.g.

$$\Delta p = \frac{1}{2}\rho \left(v_o^2 - v_i^2 \right). \tag{3}$$

Here, Δp represents the difference in pressure (or relative pressure) between two points, $\mathbf{q}_i$ and $\mathbf{q}_o$, with v_i and v_o being fluid velocity at each point. Importantly, in instances of 3D flow, velocities are projected into the direction, $\mathbf{n}$, of interrogation, reducing the 3D flow back into an assumed unidirectional equivalent. The simplicity of the RB formula, makes it an attractive approach despite some theoretical limitations.

In cases of more dominant transient flow, the so-called unsteady Bernoulli (UB) formulation [39] provides a simple extension. Returning to Eq. 1, but still assuming negligible viscous impact, relative pressure can be expressed as

$$\Delta p = \rho \int_0^1 \left(\mathbf{v} \cdot \nabla \mathbf{v} + \frac{\partial}{\partial t}\mathbf{v} \right) \bigg|_{\mathbf{x}=\mathbf{p}(s)} \cdot \frac{\partial \mathbf{p}}{\partial s} \, ds. \tag{4}$$

In this case, Δp between $\mathbf{q}_i$ and $\mathbf{q}_o$ is computed by integrating over an arbitrary integration line $\mathbf{p}(s)$ (where s is a spatial parameterization such that $\mathbf{p}(0) = \mathbf{q}_i$ and $\mathbf{p}(1) = \mathbf{q}_o$). This is sometimes denoted a *full Euler* form of the UB approach [19], incorporating temporal and spatial derivatives in the computation of Δp.

The above is *not* the commonly deployed form of UB, where clinical usage - often through the form of Doppler echocardiography - limits applicability of Eq. 4. Instead, by assuming the integration line follows a *physiological streamline*, the expression can be simplified to the common UB form, e.g.

$$\Delta p = \frac{1}{2}\rho \left(v_o^2 - v_i^2 \right) + \rho \int_0^1 \frac{\partial \mathbf{v}}{\partial t} \cdot \frac{\partial \mathbf{p}}{\partial s} \, ds. \tag{5}$$

Notice here how the advective term takes on an RB form (cf. Eq. 3), whereas the transient temporal flow derivative remains to be evaluated along the integration line.

An alternative approach is the virtual Work-Energy Relative Pressure (νWERP) technique, enabling incorporation of complete fluid flow fields to estimate pressure [17, 40, 41]. νWERP originates from Eq. 1, from which a virtual work-energy form can be achieved by multiplying with an auxiliary virtual field $\mathbf{w}$, and evaluating the resulting expression over the entire fluid domain Ω (with boundaries Γ and normal $\mathbf{n}$). With details provided in [17], relative pressure can then be expressed as

$$\Delta p = -\frac{1}{Q} \left(\frac{\partial K_e}{\partial t} + A_e + V_e \right), \tag{6}$$

with

$$K_e = \rho \int_\Omega \mathbf{v} \cdot \mathbf{w} \, d\Omega, \quad A_e = \rho \int_\Omega (\mathbf{v} \cdot \nabla \mathbf{v}) \cdot \mathbf{w} \, d\Omega, \quad V_e = \mu \int_\Omega \nabla \mathbf{v} : \nabla \mathbf{w} \, d\Omega, \quad Q = \int_{\Gamma_i} \mathbf{w} \cdot \mathbf{n} \, d\Gamma.$$

Each term above represents different *virtual* energy component within a global work-energy balance: K_e the *virtual* kinetic energy, A_e the *virtual* advective energy rate, V_e the rate of *virtual* viscous energy dissipation, and Q the *virtual* flow of $\mathbf{w}$ through the inlet plane Γ_i. Note that Δp is the change in pressure between Γ_i and Γ_o. Importantly, all terms in Eq. 6 can be directly derived from an acquired 3D velocity field $\mathbf{v}$. The only additional component needed is the numerical creation of $\mathbf{w}$, which can be any arbitrary solenoidal field where $\mathbf{w} = 0$ on domain boundaries (excluding Γ_i and Γ_o) [17].

2.2. In-silico validation of cerebrovascular relative pressure estimates

To systematically evaluate the performance of the estimation techniques in a cerebrovascular setting, a set of *in-silico* tests were performed. Anatomically accurate Computational
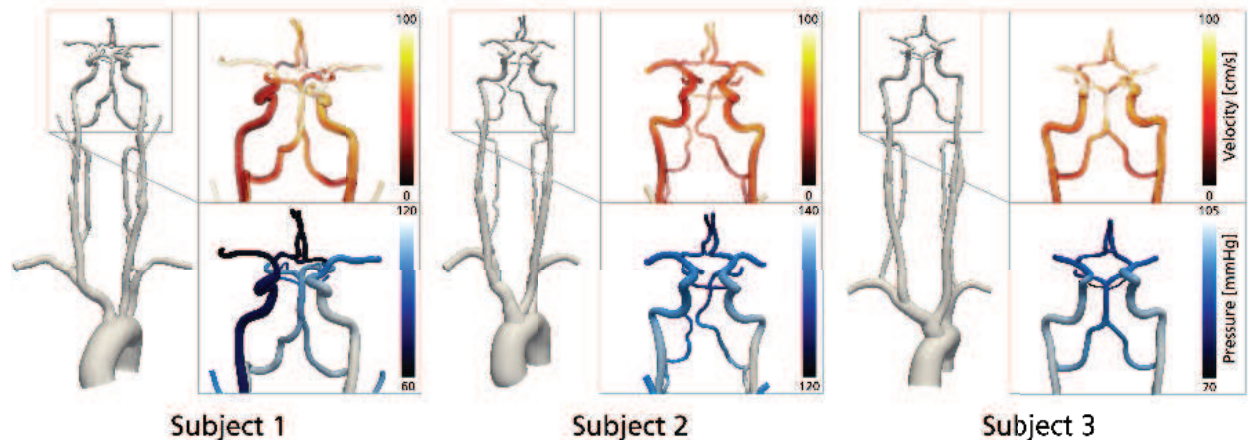
Figure 1: Velocity (top row) and pressure fields (bottom row) from the three patient-specific *in-silico* models. Models are shown front-facing, rendered around peak systole. The magnified inserts highlight the cranial-most sections used for cerebrovascular relative pressure analysis. Note that the color ranges fade into white at the upper end, with surface opacity added for visibility

Fluid Dynamics (CFD) models tailored to patient data were used to provide realistic flow and pressure fields [42].

2.2.1. Model creation and numerical setup

Using a combination of time-of-flight (TOF) MRI, 2D phase-contrast (PC) MRI, and MRI arterial spin labeling (ASL) [42], patient-specific models of the large intracranial arteries were generated, going from the aortic root to the entry section of the circle of Willis (CoW) (see Figure 1). A pulsatile flow waveform, derived from PC-MRI, was prescribed at the inlet of the aortic root. 3-element Windkessel lumped-parameter models were connected to each model outlet (descending aorta, right and left subclavian arteries, external carotid arteries (ECA), middle cerebral arteries (MCA), anterior cerebral arteries (ACA), posterior cerebral arteries (PCA), and superior cerebellar arteries (SCA)), capturing resistances and compliances of the distal vasculature. The Windkessel model parameters at the intracranial outlets were specified using a calibration strategy based on brain tissue perfusion measurements from ASL [43]. The remaining Windkessel model parameters were calibrated using local PC-MRI measurements. CFD modeling and analysis were performed using the validated open-source framework CRIMSON [44]. 3D models were meshed using tetrahedral elements. The incompressible Navier-Stokes equations solved iteratively for velocity and pressure using a stabilized finite-element formulation. Simulations were run for 5 cardiac cycles to ensure periodicity and data was extracted for the very last cycle. A detailed description of the modeling steps, including model validation, can be found elsewhere [43].

Models were generated for three subjects:

Subject 1 presented with a severe stenosis in the right proximal internal carotid artery

(ICA, 70-99% based on duplex ultrasound, velocity criteria) and a complete CoW.

Subject 2 presented with bilateral carotid stenosis (80-90% in the right proximal ICA and 60% in the left proximal ICA based on Computed Tomography Angriography (CTA) and the European Carotid Surgery Trial (ECST) criteria). The CoW was incomplete with the right P1 segment and distal right vertebral artery hypoplasia.

Subject 3 presented without evidence of cerebrovascular disease and an incomplete CoW (right and left posterior communicating artery hypoplasia).

2.2.2. Spatiotemporal analysis of cerebrovascular relative pressure estimates

To generate synthetic flow-images, CFD output was sampled onto a uniform voxelized grid. To evaluate spatiotemporal dependence in relative pressure estimates, images for Subject 1 were generated over a range of spatiotemporal samplings, including $dx = 1, 0.75, 0.5,$ and 0.25 mm isotropic, and $dt = 80, 40,$ and 20 ms, respectively (see Figure 2). These levels were purposely selected to cover clinical image ranges, as well as including resolutions beyond current clinical practice.

For each model, relative pressure was estimated over four sections: *Left / Right ICA*, representing a section going from the cranial end of the cervical ICA, to the mid-section of the petrous ICA (being a non-bifurcated section including a close-to 90° bend, see section A-B (right) and D-E (left) in Figure 2); and *Left / Right ICA-MCA*, representing a section starting from the outlet plane of the ICA, and ending at the mid-way of the horizontal
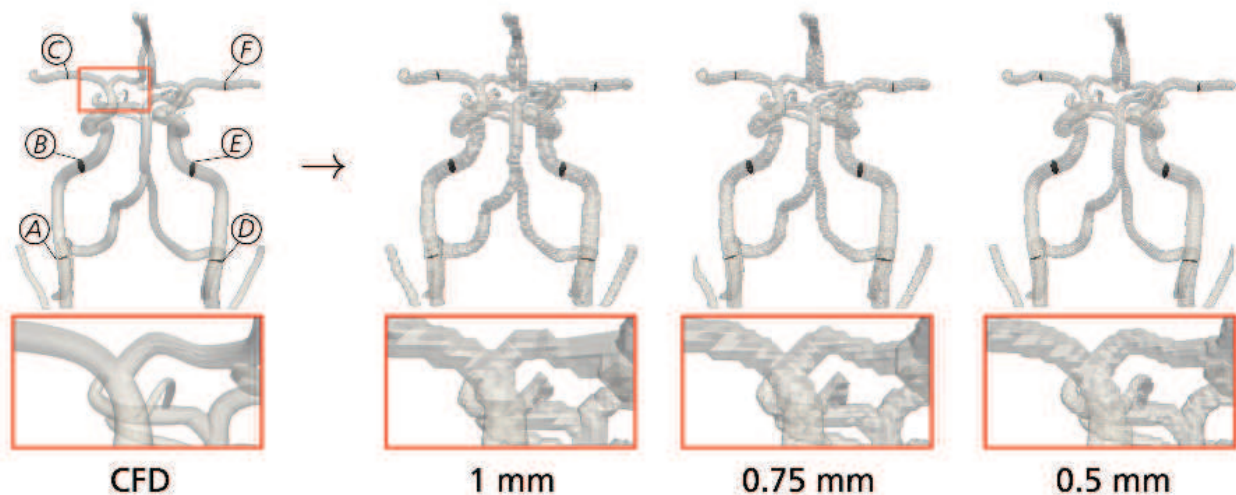
Figure 2: Generation of *in-silico* image data from the patient-specific CFD simulations. From left to right: the CFD model, with planes isolating the vascular segments of interest highlighted (A through F); the generated voxelized model at 1 mm, 0.75 mm, and 0.5 mm, respectively, showing how the anatomy gets resolved at increasing detail. The inserts in red shows a magnification of the bifurcation of the right ICA into the MCA and the right anterior cerebral artery.

segment (M1) of the MCA (including the tortuous bends of the cavernous ICA, as well as the MCA-ACA bifurcation, see section B-C (right) and E-F (left) in Figure 2).

For all sections and samplings, relative pressures were estimated using RB, UB, and νWERP. For RB, peak velocities were extracted from the inlet and outlet plane, whereas UB was evaluated along the centerline of the vessel. Ground truth relative pressure was provided by the CFD pressure field, sampled onto an identical image grid.

2.2.3. Inter-subject validation and noise sensitivity analysis

To evaluate accuracy over different models, an inter-subject validation test was performed. Data from Subjects 1-3 were included, sampled using $dx = 1.0$ and 0.5 mm, and $dt = 40$ ms (with spatiotemporal levels chosen after analysis in Section 2.2.2). ICA and ICA-MCA planes for Subjects 2 and 3 were created analog to Subject 1.

To additionally assess the effect of random image fluctuations, synthetic image noise was added to the generated data. By assigning a synthetic velocity encoding of $v_{enc} = 140$ cm/s, and knowing that v_{enc} relates to velocity standard deviation σ and signal-to-noise-ratio (SNR) as

$$\sigma = \frac{\sqrt{2}v_{enc}}{\pi \cdot SNR},\tag{7}$$

σ could be derived for three different noise-scenarios: low-noise (SNR = 30), mid-noise (SNR = 20) and high-noise (SNR = 10). Noise was distributed over all voxels and all frames using a truncated Gaussian distribution (truncation at $[-2\sigma, 2\sigma]$). For each image set, 25 different noise fields were generated, for which relative pressures were assessed using RB, UB, and νWERP, respectively.

2.3. In-vivo feasibility study of cerebrovascular relative pressure estimates

To showcase clinical applicability, and to infer possible correlations between resolutions in a clinical setting, in-vivo 4D Flow MRI was collected and analyzed in a separate cohort. A study cohort consisting of 8 healthy volunteers (2 women, 55 ± 18 years) with no known history of cerebrovascular disease were selected. The acquisitions were performed as part of an institutional review board (IRB) approved study including informed consent, with data collected in retrospective fashion.

2.3.1. Imaging protocol

The MRI acquisition was performed using a 3T scanner (Siemens Magnetom Skyra, Erlangen, Germany) equipped with a 20-channel head/neck coil, with supportive cushions used to fixate the subjects' head within the scanner. Acquisition started with a 3D time-of-flight (TOF) MRA sequence (TR = 21 ms; TE = 3.6 ms; flip angle = 18°; acquired resolution

dx 0.5x0.5x1.0 mm with scanner reconstruction to $dx = 0.25$x0.25x0.5 mm; approximate scan time = 5:30 minutes), centering the field-of-view around the CoW and including the proximal parts of the bilateral intracranial ICAs and bifurcations into MCAs and ACAs. 4D Flow MRI was acquired using a prospectively ECG-gated k-t GRAPPA accelerated dual-venc sequence (high-venc (130 cm/s) used for anti-aliasing correction of the low-venc (45 cm/s) equivalent) [45]. Data was corrected for concomitant gradients fields, eddy currents, and noise [45, 46, 47]. To evaluate dependence on spatial resolution, scans were performed at two different resolutions: $dx = 1.1$ mm ($dt = 95$ ms; TR = 6.80 ms; TE = 3.97 ms; flip angle = 15°; inversion time = 150 ms; approximate scan time = 15:35 minutes with an acceleration factor = 2) and 0.8 mm ($dt = 104$ ms; TR = 7.40 ms; TE = 4.37 ms; flip angle = 15°; inversion time = 150 ms; approximate scan time = 12:35 minutes with an acceleration factor = 5) isotropic, respectively. (representative examples are given in Figure 3).

2.3.2. Image processing and relative pressure estimation

Vessel segmentation, and identification of centerlines and cross-sectional cut planes were generated using a previously published analysis framework (utilizing threshold segmentation of the 3D TOF MRA data, and rigid co-registration of the 4D Flow MRI data) [18, 48].

To assess relative pressures, ICA-MCA sections comparable to those defined for the *in-silico* models were manually identified. This was achieved by identifying anatomical landmarks, defining an inlet plane at the transition between the petrous and the cavernous section of the ICA, and defining an outlet plane at the mid-way of M1-segment of the MCA. From these landmarks, the closest-most cross-sectional plane from the centerline procedure was selected as the plane-of-interest. Identified planes were visually co-aligned at the different image resolutions to ensure comparable output. Due to the limited field-of-view, ICA-sections comparable to those in Section 2.2 could not be extracted. Relative pressure was estimated using RB, UB, and νWERP.
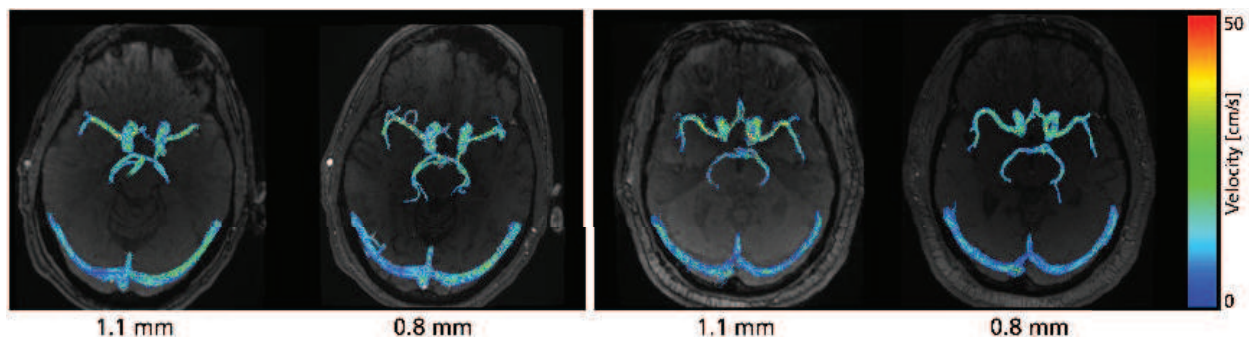
Figure 3: Representative 4D Flow MRI from two volunteer subjects, shown both at $dx = 1.1$ and 0.8 mm, respectively. Note how varying number of side-branches are detected during segmentation in the different datasets (velocity range given as [0-0.5] m/s).

2.4. Statistical analysis

For the *in-silico* analysis, estimation of mean similarity between output and ground truth was calculated by the normalized Fréchet distance, d_f, given as

$$d_f = \frac{\inf_{\Delta p, \Delta p_e} \max_{t \in [t_0, t_n]} ||\Delta p(t) - \Delta p_e(t)||}{\inf_{\Delta p} \max_{t \in [t_0, t_n]} ||\Delta p(t)||}. \tag{8}$$

Here, Δp is the true relative relative pressure given by the CFD solution, and Δp_e is the corresponding estimated output. d_f thus measures the *average distance* between Δp and Δp_e over the entire temporal cycle T, with the metric normalized by the distance between Δp and a reference null-estimate. As such, d_f is unbounded from 0% (representing a perfect 1:1 match between Δp_e and Δp) to above 100% (representing a scenario where Δp_e generates larger errors than an effective null-estimate of $\Delta p_e = 0$). In all instances, Δp_e and Δp were linearly upsampled to the highest temporal sampling (10 ms), with reference Δp given by the solution at that highest sampling.

Errors in maximum relative pressure were evaluated as

$$\varepsilon(\Delta P_{max}) = \left(\frac{|\Delta p_e(t_m) - \Delta p(t_m)|}{|\Delta p(t_m)|} \right), \tag{9}$$

where t_m is the time at maximum relative pressure of the true estimate Δp.

For both the *in-silico* and *in-vivo* evaluation, linear regression analysis was performed between predicted and true pressure drop, along with a Bland-Altman assessment. Complete data analysis was performed in MATLAB R2016a (MathWorks, Natick, MA, USA).

3. Results

3.1. In-silico validation of cerebrovascular relative pressure estimates

3.1.1. Spatiotemporal analysis

Output data for the relative pressure estimation through all evaluated vascular sections in Subject 1 are provided in Table 1, showing d_f and ε_{max} for RB, UB, and νWERP, respectively. Example output of relative pressure over two selected sections (right ICA, and right ICA-MCA) are provided in Supplementary Information Figure S.1.

For all estimation approaches, errors decrease with increasing spatiotemporal sampling. At the coarsest resolution ($dx = 1$ mm, $dt = 80$ ms), $d_f = 79.2, 65.0$, and 45.0% for RB, UB, and νWERP, respectively, whereas at the highest resolution ($dx = 0.25$ mm, $dt = 10$ ms), $d_f = 56.8, 39.8$, and 10.1%. Consequently, increasing sampling from lowest to highest renders a decrease in error by a factor of 1.4, 1.6, and 4.5 for RB, UB, and νWERP, respectively.

Table 1: Numerical data for the estimation of relative pressure through the cerebrovascular sections of Subject 1, given for RB (first from left), UB (second from left), and νWERP (third from left), respectively. Results are presented for the normalized Fréchet distance d_f (top rows), and for the maximum relative error ε_{max} (bottom rows), with data shown as a function of spatial and temporal image sampling. Note that results are given as a mean average over all four evaluated cerebrovascular sections (right and left ICA, and right and left ICA-MCA, as per Section

RB					UB					νWERP				
d_f					**d_f**					**d_f**				
dx \ dt	80 ms	40 ms	20 ms	10 ms	dx \ dt	80 ms	40 ms	20 ms	10 ms	dx \ dt	80 ms	40 ms	20 ms	10 ms
1 mm	79.2	68.6	67.5	82.3	1 mm	65.0	65.3	63.8	79.2	1 mm	45.0	28.0	24.7	21.6
0.75 mm	77.2	65.9	64.5	63.8	0.75 mm	65.0	61.9	60.6	59.9	0.75 mm	31.9	12.2	11.3	8.5
0.5 mm	76.7	68.9	70.0	70.7	0.5 mm	69.5	71.5	69.5	67.9	0.5 mm	31.4	10.7	10.4	5.8
0.25 mm	73.3	59.0	58.2	56.8	0.25 mm	59.4	49.5	46.3	39.8	0.25 mm	30.8	9.8	10.5	10.1
ε_{max}					**ε_{max}**					**ε_{max}**				
dx \ dt	80 ms	40 ms	20 ms	10 ms	dx \ dt	80 ms	40 ms	20 ms	10 ms	dx \ dt	80 ms	40 ms	20 ms	10 ms
1 mm	75.2	70.4	69.4	75.7	1 mm	61.4	58.6	51.4	44.9	1 mm	26.8	23.4	19.5	18.1
0.75 mm	74.9	68.6	71.1	71.4	0.75 mm	61.3	58.7	53.6	54.7	0.75 mm	7.8	9.1	10.5	8.2
0.5 mm	76.1	67.1	67.1	67.3	0.5 mm	62.2	55.2	48.4	49.5	0.5 mm	5.4	4.1	6.6	4.4
0.25 mm	63.4	60.8	63.1	63.5	0.25 mm	54.5	52.6	47.4	48.1	0.25 mm	3.8	3.6	4.8	2.5

2.2

νWERP exhibited highest accuracy, with $d_f < 12.2\%$ for all samplings of $dx \leq 0.75$mm and $dt \leq 40$ms. In contrast, both RB and UB report consistently higher errors even at fine sampling, with d_f and $\varepsilon_{max} > 50\%$ over almost all evaluated resolutions.

With respect to spatiotemporal tendencies, νWERP exhibited no strong favoring of spatial or temporal refinement over the entire evaluated range: a twofold increase in spatial sampling (1 to 0.5, or 0.5 to 0.25 mm) rendered an average decrease in d_f by 20%, whereas a twofold increase in temporal sampling (80 to 40, or 40 to 20 ms) renders an average decrease in d_f by 28%. However, for all data at which $dt \leq 40$ ms, a stronger dependency on spatial resolution is evident (twofold temporal vs. twofold spatial increase rendering a decrease in d_f by 12 vs. 21%, respectively). For RB and UB, only marginal improvements are observed with increasing spatiotemporal resolution, notably when using the highest sampling (for which $d_f = 56.8\%$ and 39.8% for RB and UB, respectively).

Linear regression plots are given in Figure 4. At $dx = 1$ mm systematic underestimation bias is evident in all three methods (linear regression slope $k = 0.44$, 0.46, and 0.55 for RB, UB, and νWERP, respectively). As spatial sampling increases, slopes are increased, however, accurate estimates are only achieved using νWERP: at $dx = 0.25$ mm, $k = 0.49$, 0.51, and 1.01 for RB, UB, and νWERP. Different trends also seem evident for different vascular sections. The RICA-RMCA and LICA-LMCA sections (green and yellow in Figure 4) exhibit different regression slopes for RB and UB over all spatial ranges (RICA-RMCA having on average $k = 0.64$ and 0.66 for RB and UB, vs. LICA-LMCA having on average $k = 0.34$ and 0.40), and the relationship between resolutions also vary as a function of assessed vascular section. For νWERP, the same separation is not visible at higher resolution, however at $dx = 1$ mm, the non-bifurcated ICA sections (blue and red in Figure 4) have distinctly
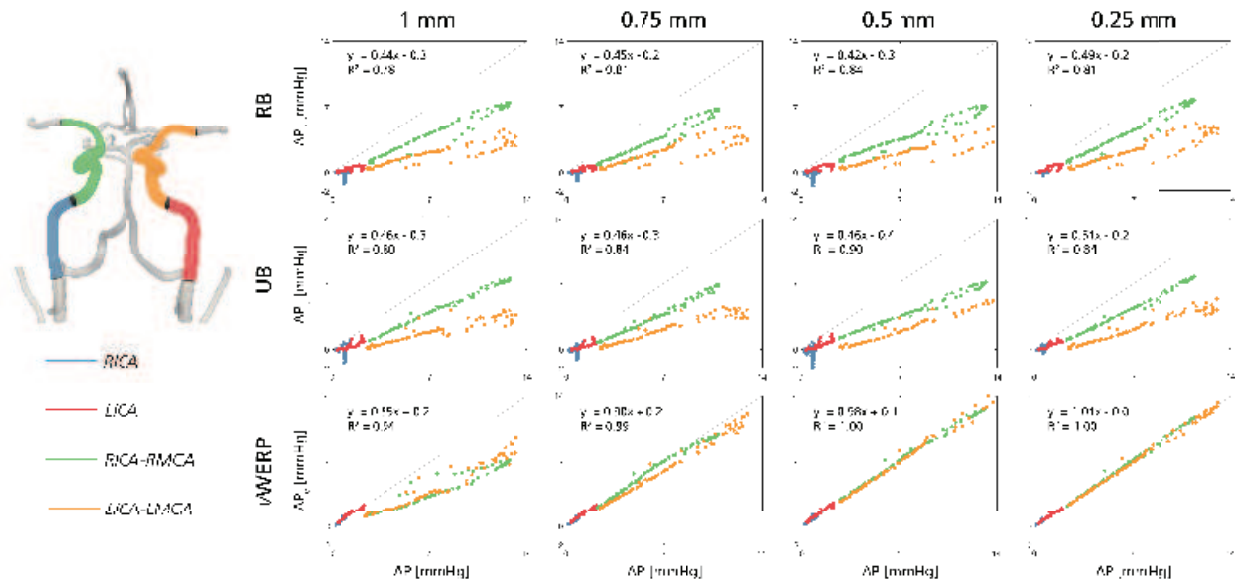
Figure 4: Linear regression plots for the spatiotemporal convergence analysis, assessing relative pressures through selected cerebrovascular sections of Subject 1. To highlight differences between vascular sections, each section is given as a separate color (RICA in blue; LICA in red; RICA-RMCA in green; LICA-LMCA in yellow), where each data point represents an estimated relative pressure at a specific discrete time point. Results are shown for incremental refinements in spatial sampling (dx = 1-0.25 mm), however, pooled for all variations in temporal sampling (dt = 80-20 ms). Results are separated from top to bottom by using RB, UB, and νWERP, respectively.

different regression slopes compared to the ICA-MCAs ($k = 1.04$ for RICA/LICA vs. $k = 0.65$ for RICA-RMCA/LICA-LMCA). Still, the relationship between resolutions varies as a function of assessed vascular section.
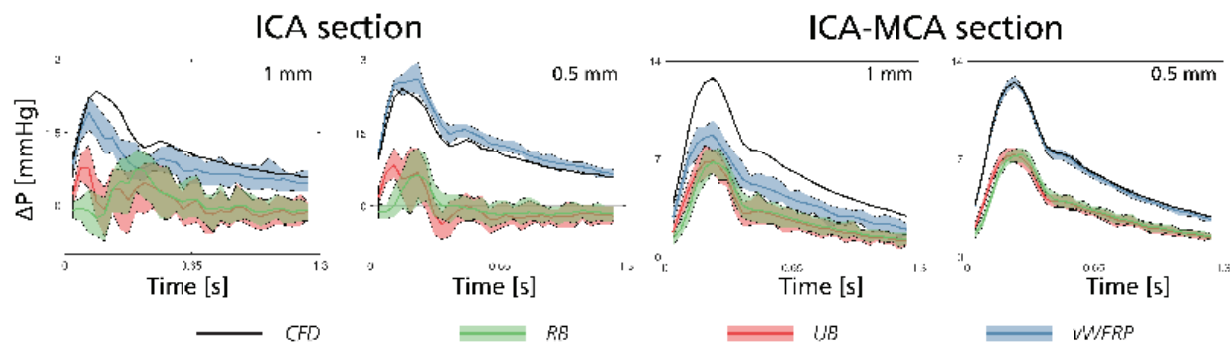
Figure 5: Relative pressure traces through Subject 3, shown for the left ICA (left) and LICA-LMCA (right) section, respectively, at a high-noise configuration (SNR = 10). For both sections, results are shown for dx = 1 mm and 0.5 mm. In each graph, data is shown for reference CFD (black), RB (green), UB (red), and νWERP (blue), with the shaded areas showing the extent over all evaluated noise tests ($n = 25$).

Table 2: Noise sensitivity analysis, performed over all *in-silico* subjects. Results are presented in the top rows for the normalized Fréchet distance d_f, estimating the mean similarity between estimated and true relative pressure, and in the bottom rows for the maximum relative error ε_{max}. Furthermore, results are provided separately for $dx = 1.0$ vs. 0.5 mm.

		RB		**UB**		ν**WERP**	
		d_f		**d_f**		**d_f**	
SNR	**dx**	**1.0 mm**	**0.5 mm**	**1.0 mm**	**0.5 mm**	**1.0 mm**	**0.5 mm**
30		75.2 ± 5.8	76.7 ± 4.6	67.2 ± 5.8	68.3 ± 4.6	25.4 ± 3.1	8.1 ± 0.9
20		74.4 ± 9.0	76.3 ± 6.7	66.6 ± 8.9	68.3 ± 6.9	25.2 ± 4.8	8.1 ± 1.3
10		71.8 ± 15.4	73.4 ± 15.8	66.3 ± 17.2	66.8 ± 15.9	25.0 ± 7.7	8.6 ± 2.9
		ε_{max}		**ε_{max}**		**ε_{max}**	
SNR	**dx**	**1.0 mm**	**0.5 mm**	**1.0 mm**	**0.5 mm**	**1.0 mm**	**0.5 mm**
30		77.7 ± 5.4	74.4 ± 3.9	58.3 ± 5.7	65.4 ± 4.1	27.2 ± 4.1	4.7 ± 1.4
20		77.4 ± 6.5	74.2 ± 5.5	66.4 ± 6.7	65.2 ± 5.8	27.6 ± 6.1	4.6 ± 2.1
10		76.4 ± 12.8	74.1 ± 10.7	65.2 ± 13.3	65.0 ± 11.1	28.1 ± 11.5	4.8 ± 3.9

3.1.2. Inter-subject validation and noise sensitivity

For the inter-subject validation and noise sensitivity analysis, d_f and ε_{max} are given in Table 2, shown for increasing SNR.

Overall, the addition of noise does not significantly impact the accuracy in estimated relative pressure: between a high- and low-noise configuration (SNR = 10 vs. 30), d_f and ε_{max} changes by <7% over all evaluated estimation methods, respectively (see Table 2). This
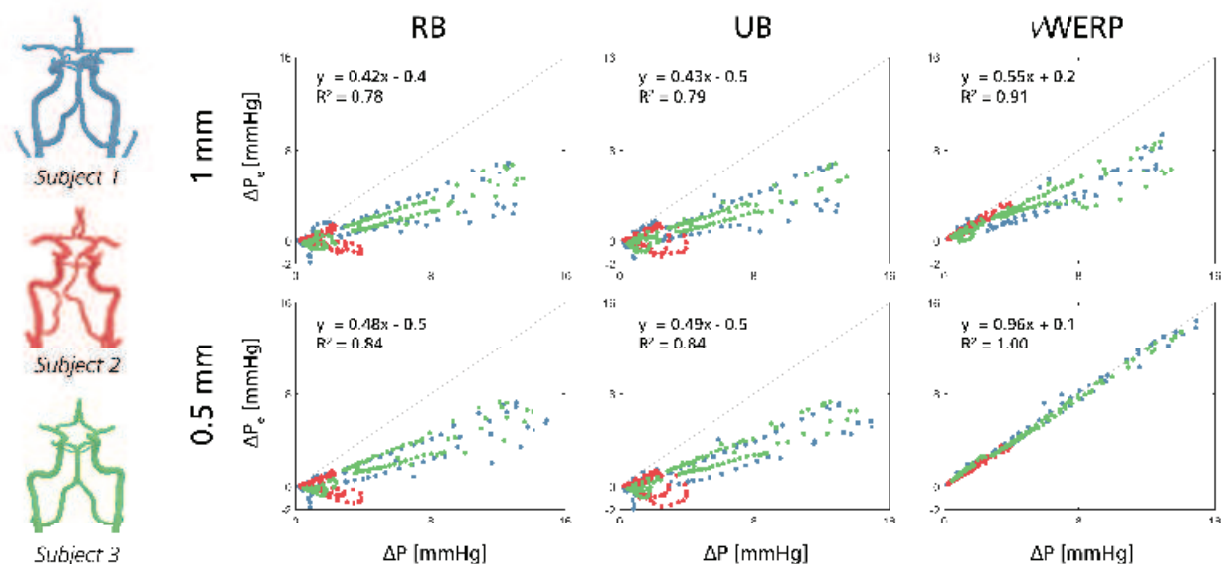
Figure 6: Linear regression plots for the inter-subject validation study, shown for the high-noise configuration (SNR = 10). Results are shown for RB, UB, and νWERP, with estimates evaluated at $dx = 1.0$ (top row) and 0.5 mm (bottom row), respectively. Furthermore, data from each subject is given a specific color (Subject 1 in blue, Subject 2 in red, Subject 3 in green).

behavior is also visually apparent in Figure 5, showing example output of relative pressures in Subject 3. Furthermore, the dependency on spatial resolution observed in Section 3.1.1 seem to be maintained even with the inclusion of image noise. As presented for a high-noise configuration (SNR = 10) in Figure 6, all methods exhibit underestimation bias at $dx = 1$ mm (linear regression slope of $k = 0.42$, 0.43, and 0.55 for RB, UB, and νWERP, respectively, at SNR = 10). At $dx = 0.5$ mm, the underestimation persists for RB and UB, however diminishes for νWERP ($k = 0.96$ at SNR = 10).

3.2. In-vivo assessment of cerebrovascular relative pressure estimates

In-vivo relative pressure traces through the LICA-LMCA section of a selection of study subjects are provided Figure 7. Bland-Altman plots comparing output at $dx = 1.1$ and 0.8 mm for all eight subjects are provided in Figure 8. Linear regression plots of the same data is also given in Supplementary Information Figure S.2).

For νWERP, estimates are within the range of 0-7 mmHg (see Figure 8), with peak relative pressures at 2.9 ± 1.7 mmHg at $dx = 1.1$ mm, and 3.8 ± 1.8 mmHg at $dx = 0.8$ mm. No differences are observed between right and left ICA-MCA (peak relative pressure in right vs. left-hand ICA-MCA being 3.3 ± 1.8 vs. 4.3 ± 1.8 mmHg at $dx = 0.8$ mm). Estimates are consistently lower at $dx = 1.1$ mm with an average shift of around 0.9 mmHg.

For RB and UB, lower peak relative pressures are observed (for RB: 1.3 ± 1.3 mmHg at $dx = 1.1$ mm, vs. 1.3 ± 1.3 mmHg at $dx = 0.8$ mm; for UB: 1.5 ± 1.3 mmHg at $dx = 1.1$ mm, vs. 1.5 ± 1.2 mmHg at $dx = 0.8$ mm), however, again with no distinct difference between right and left-hand side ICA-MCA. Furthermore, no specific bias is observed between the two resolutions (mean average shift of $m = -0.2$ between $dx = 1.1$ vs. 0.8 mm), although, no correlation is observed between the two resolutions ($k < 0.1$ for both RB and UB, see Supplementary Information Figure S.2).
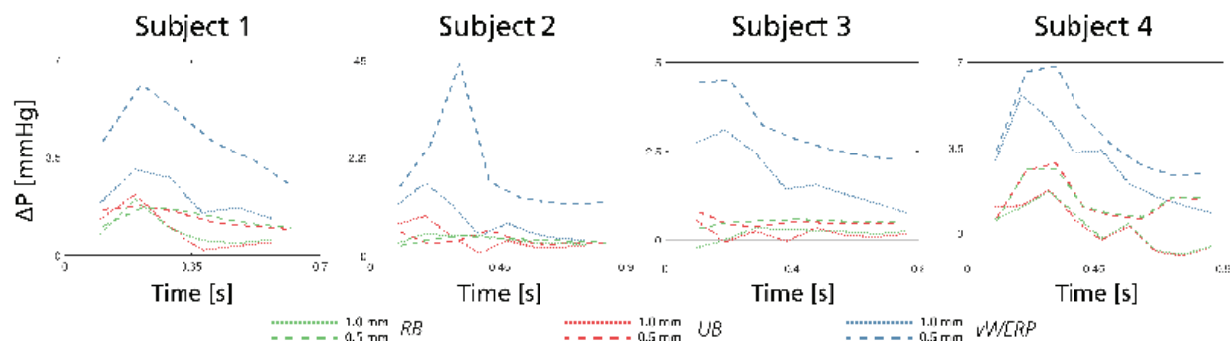
Figure 7: Traces of relative pressure through the LICA-LMCA section of four subjects, shown for RB (green), UB (red), and νWERP (blue), respectively. For each method, estimates are provided at $dx = 1.1$ mm (dotted) and $dx = 0.8$ mm (dashed), respectively.
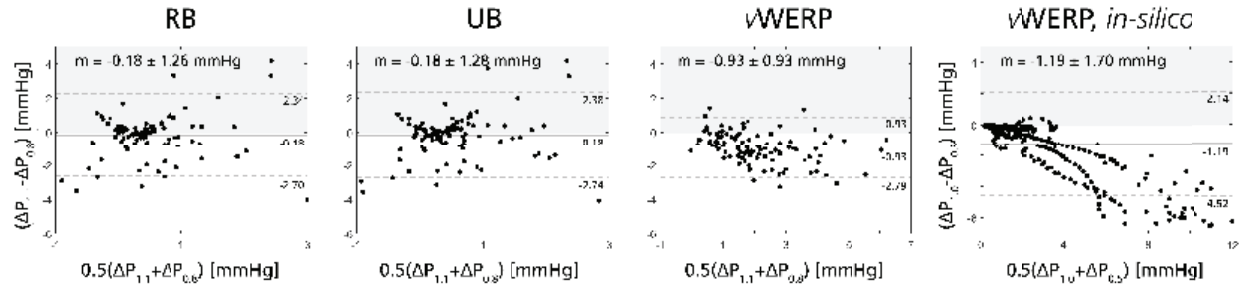
Figure 8: Bland-Altman plots comparing relative pressure estimates for all eight subjects, obtained at dx = 1.1 vs. 0.8 mm using RB, UB, and νWERP, respectively. For reference, νWERP results at dx = 1.0 vs. 0.5 mm from the *in-silico* tests (Section 3.1) are shown at the far right.

For reference, Bland-Altman data for the νWERP estimates at dx = 1.0 vs. 0.5 mm for the *in-silico* datasets (from the tests in Section 3.1.2) is also provided in Figure 8.

4. Discussion

In this study, we evaluated the use of 4D Flow MRI to quantify cerebrovascular relative pressure. Using patient-specific *in-silico* models, we showed that accurate estimates can be achieved, but that they depend on both utilized image resolution and estimation approach: at $dx < 0.75$ mm νWERP recovers relative pressures at high accuracy, whereas a persistent underestimation bias seem to prevail for the Bernoulli-based techniques regardless of resolution. This behavior is also indicated *in-vivo*, underlining the implications of our findings. Our study thus illustrates the potential benefits and challenges of using 4D Flow MRI to quantify cerebrovascular relative pressure.

4.1. Quantification and validation of image-based cerebrovascular relative pressure mapping

4.1.1. Full-field νWERP estimation

From the *in-silico* analysis, νWERP - a method originating from a full-field fluid mechanical description, and avoiding having any major assumptions imposed on the imaged flow - proved to be the most effective in accurately probing relative pressure. Still, results underline how accuracy is directly dependent on sufficient spatiotemporal sampling.

Systematic underestimation seemed evident at $dx = 1$ mm, whereas accuracy improved distinctly for $dx \leq 0.75$ mm: relative errors being consistently kept <10%, absolute errors being <0.5 mmHg, and a virtual 1:1 correlation recovered between true and estimated data at $dx \leq 0.5$ mm. Importantly, at $dx \leq 0.5$ mm, accurate estimates were achieved through all sections, in all subjects, and over all noise-levels, highlighting general applicability of the method. Mild dependency was also observed with respect to temporal sampling, however these effects were only minor for $dt \leq 40$ ms. As such, our observations indicate that *spatial*

features drive cerebrovascular relative pressure, including spatial flow paths and flow gradients, and that emphasize should be given to spatial sampling when attempting to quantify cerebrovascular relative pressures.

Interestingly, this spatial dependency seems most pronounced in the ICA-MCA sections, where the narrower and more tortuous anatomy (as compared to the straighter ICA-sections) makes the relative pressure estimates more dependent on accurate spatial sampling. As such, if probing predominantly larger cerebrovascular vessels (the cervical ICA, the dural sinuses) lower resolution could suffice, still, increased spatial sampling should be prioritized if permitted.

4.1.2. Reduced-field Bernoulli-based estimates

In comparison, both Bernoulli-based methods reported higher errors throughout the *in-silico* tests. Output data also indicate inherent obstacles associated with Bernoulli-based estimations, with only minor improvements observed with increasing spatiotemporal sampling, and pronounced errors reported over all noise levels. Importantly, data also shows how the relationship between Bernoulli-based estimates and ground truth data varies as a function of probed vascular section (Fig. 4), evaluated subject (Fig. 5), and between different resolution levels. This highlights how RB or UB errors cannot simply be compensated for by a systematic correction shift, but that it has to be tailored for each single subject and vessel section evaluated, respectively. To appreciate these observed deviations, it is imperative to understand the fundamental model assumptions of both RB and UB:

As outlined in Section 2.1, RB is based on a number of assumptions that might not hold true in the cerebrovasculature. Firstly, transient and viscous effects are assumed negligible, meaning that the method is not optimized to capture temporal variations in relative pressure. Secondly, RB assumes unidirectional flow, where complex 3D motion is reduced to the peak velocity estimates of Eq. 3. Whilst this might hold true in instances of fast flowing blood ejected through narrow sections, the same might not be said throughout the tortuous cerebrovasculature, and estimation bias is frequently reported even under idealized flow settings [15, 16, 18]. Our findings thus corroborate difficulties associated with RB, and highlight challenges associated with using the approach in the cerebrovasculature.

UB comes with fewer assumptions, however still reduces evaluation to an integration line $\mathbf{p}(s)$ as per Eq. 5. As outlined in Section 2.1, this only holds true when $\mathbf{p}(s)$ follows a *physiological streamline* [49], and if instead using a user-defined integration line (e.g. the vessel centerline) the conversion from Eq. 4 to Eq. 5 is no longer valid. In fact, if reverting back to the full Euler form provided in Eq. 4 - where method output is no longer dependent on the choice of integration path - distinct improvement in method accuracy is observed (see

Supplementary Information S.2), highlighting that it is indeed the choice of integration line that obstructs UB accuracy. Nevertheless, reported errors for the full Euler UB approach are still comparably larger than those reported using νWERP, highlighting that viscous effects - overlooked in any of the UB formulations - play a noticeable role in the development of relative pressure in the brain.

4.2. In-vivo feasibility and clinical contextualization

In Section 3.2, cerebrovascular relative pressures were derived in an *in-vivo* cohort. Although ground truth pressure measurements were unavailable, the trends observed *in-silico* were also mirrored *in-vivo*. Firstly, Bernoulli-based estimates report no specific bias, although also no observable correlation between different spatial resolutions (see Supplementary Information Figure S.2, with $k < 0.1$ and $R^2 < 0.1$, for both RB and UB comparing dx = 1.1 vs. 0.8 mm), indicating inherent difficulties in reliably extracting cerebrovascular relative pressure. Secondly, νWERP generates more physiological observable features (systolic peaks in relative pressure seen over multiple subjects in Figure 7), whilst still highlighting dependency on spatial resolution. In fact, νWERP output behaves in a very similar manner as observed in the corresponding *in-silico* data (both in Figure 8 and Supplementary Information Figure S.2), underlining the plausibility of these findings.

Comparing *in-silico* and *in-vivo* further, estimated relative pressure *in-vivo* ranges up to 7 mmHg, whereas corresponding *in-silico* data spans almost 15 mmHg. Direct comparison between the two datasets is challenging, with the two originating from different cohorts with different underlying anatomies, disease, and even acquisition settings. Still, these observed discrepancies could occur for a number of reasons. Firstly, even though *in-vivo* vascular sections were selected to mimic those chosen *in-silico*, the field-of-view of the *in-vivo* scan did occasionally not include the petrous section of the ICA. In these cases, a more caudal plane was selected, resulting in a shorter vascular domain and possibly lower relative pressures. Secondly, the *in-vivo* cohort consisted of exclusively healthy volunteers, whereas the *in-silico* models included moderate-to-severe stenoses on caudal sections of the ICA; features known to generate increased pressure changes. Lastly, the *in-silico* data represents an idealization of the *in-vivo* equivalent, where acquisition inaccuracies might influence the *in-vivo* data to an extent not covered by the simulated data. Likewise, it should be noted that neither of the *in-vivo* resolutions were within what was noted to be sufficient spatial sampling (i.e. $dx <$ 0.75 mm), and with previous studies indicating how acquiring 4D Flow MRI in vessels with ≤ 3 voxels in diameter can cause a shift in flow accuracy [30], true *in-vivo* relative pressure might in fact be above those reported at $dx = 0.8$ mm. Future direct comparison between CFD-generated data and 4D Flow MRI from the very same patient could help clarify possible

discrepancies noted above.

It is worth contrasting observed findings to previously published data on cerebrovascular relative pressure. Using invasive catheterization, both Han et al. [21] and Miao et al. [22] evaluated pressure changes over larger cerebrovascular arteries before and after interventional stenting, reporting post-procedural values of around 11-13 mmHg; similar to those reported in our non-stenosed data. For image-based assessments, Vali et al [18] quantified pressure changes over stenosed cerebrovascular sections using 4D Flow MRI, with reported magnitudes of up to 5 mmHg. However, pressure estimates were extracted over highly regional sections using a Bernoulli-based approach at $dx \geq 0.8$ mm. The deviations observed in our study suggests that using RB and UB might have influenced these results. When it comes to alternative methods based on full-field data, Rivera-Rivera et al. [4] extracted relative pressures directly from the Navier-Stokes equations using 4D Flow MRI data, reporting much milder pressure changes, however, doing so in the dural sinus where significantly lower flow velocities prevail. Similarly, Zhang et al. [35] reported lower relative pressure magnitudes in aneurysmal geometries using a error-weighted PPE approach, however, acknowledged that the extension of their approach into narrower segments is limited due to the need for central difference gradient estimators. Still, assessment similar to that performed in this study (mapping spatiotemporal dependence and noise sensitivity in a cerebrovascular setting) remains to be performed for these alternative full-field techniques.

A variety of computational studies have also been performed, assessing pressure changes over diseased cerebrovascular section. Schirmer et al. [50] used CFD-modelling to assess stenosed ICA and MCA sections, indicating peak pressure drops of 27 mmHg for stenosis above 75%, with higher magnitudes reported at higher constriction [51]. For non-stenosed anatomies, Reymond et al. [52] evaluated pressure changes throughout the cardiovascular system, indicating that pronounced pressure changes are observed at the transition from ICA-MCA, with magnitudes similar to those indicated in our study (10-15 mmHg). Similarly, Blanco et al. [53] used lumped parameter modelling to describe pressure drops in the initial arterial section of the cerebrovasculature, reporting pressure drops of 18 mmHg in normotensive patients, again similar to those found in our *in-silico* data. However, an in-depth analysis of the differences between simulated and acquired data would require further study beyond the scope of this paper.

4.3. Limitations

Validations in this study were performed exclusively *in-silico*, with *in-vivo* data used to infer similar mechanisms. Thus, important experimental *in-vitro* or clinical *in-vivo* validation against invasive catheterization thus remains to be performed. However, whilst dedicated

patient-specific *in-vitro* setups are emerging [54], such testing requires infrastructure not currently available within the scope of this paper. Continuing, acquiring invasive pressure data in conjunction with *in-vivo* or *in-vivo* 4D Flow MRI comes with its own unique challenges (co-registration, catheter-induced flow disturbances), especially in the cerebrovasculature. With νWERP successfully validated in narrow adolescent aortas [17], and with alternative approaches showing limited performance in representative reference data [18, 36], the derived νWERP behavior still bears potential for improved cerebrovascular relative pressure mapping, and the purpose of this work should instead be to highlight innate dependencies on spatiotemporal resolution when probing for cerebrovascular relative pressure - present even under idealized *in-silico* settings. Nevertheless, experimental validation represents an important extension of our current work, and should be the focus of subsequent studies.

Though sampled onto an image-equivalent grid, the *in-silico* data represent an idealized version of an *in-vivo* scan. Nevertheless, the noise sensitivity analysis highlights the robustness of νWERP, in part coming from its integrative nature. Still, for clinical translation care should be taken to correct for possible spurious data points or flow field errors.

Last, even though 4D Flow MRI sequences are part of most contemporary scanners, its acquisition is not considered routine, limiting the applicability of our findings. However, as our study indicates, the complex 3D nature of cerebrovascular flow might be an incentive for including full-field imaging, in order to accurately probe hemodynamic change. Furthermore, even though the required spatial resolution derived *in-silico* ($dx < 0.75$ mm) is at the limit of what can today be achieved using routine scanners, continuous developments keeps pushing the envelope of achievable resolutions (a very recent study on intracranial 4D Flow MRI reported acquisitions at $dx = 0.5$ mm using a combination of pseudospiral Cartesian undersampling and compressed sensing reconstruction [55]). Contemporary developments in the field of machine learning also promises super-resolution abilities for 4D Flow MRI data [56], showing promise for high-resolution full-field flow imaging.

4.4. Clinical outlook

For cerebrovascular disease, diagnostic practice is still mainly driven by anatomical assessment of symptomatic patients, using aneurysmal size or stenosis degree to stratify risk [57, 58]. Several studies have however highlighted how the inclusion of flow and pressure could improve assessment [1, 59], and with the cerebrovasculature characterized by complex flow [3, 8, 9] distributing through an intricate vascular network, full-field flow imaging has the potential to provide invaluable insights into apparent disease state. When combined with an approach such as νWERP, clinically established biomarkers of relative pressure could now also be applied in a more complex cerebrovascular setting.

Even though the narrow cerebrovasculature puts certain demands on spatiotemporal sampling, the current study outlines requirements with which accurate assessments can be achieved. Furthermore, with νWERP acting directly on imaged full-field data, it serves as a viable tool bringing cerebrovascular relative pressure estimates closer to clinical reality.

5. Conclusion

We presented a systematic evaluation of image-based relative pressure mapping in the cerebrovasculature, showing how accurate estimates can be achieved using 4D Flow MRI. Our data highlights that output is directly dependent on utilized image resolution ($dx <$ 0.75 mm indicated through the CoW *in-silico*) and estimation approach (accurate estimates achieved using the full-field νWERP method, whilst consistent underestimation bias seem evident with comparable Bernoulli-based techniques). Results are also corroborated by similar findings indicated in a feasibility *in-vivo* analysis. With continued clinical validation, and with technical advancements pushing high-resolution scans into clinical practice, 4D Flow MRI in combination with νWERP thus has definite potential to provide added diagnostic value in a clinical cerebrovascular setting.

Acknowledgments

[1] X. Leng, K. S. Wong, D. S. Liebeskind, Evaluating intracranial atherosclerosis rather than intracranial stenosis, Stroke 45 (2014) 645–651.

[2] D. S. Liebeskind, A. S. Kosinski, M. J. Lynn, F. Scalzo, A. K. Fong, P. Fariborz, M. I. Chimowitz, E. Feldmann, SONIA, W. Investigators, Noninvasive fractional flow on mra predicts stroke risk of intracranial stenosis, Journal of neuroimaging 25 (2015) 87–91.

[3] D. L. Penn, R. J. Komotar, E. S. Connolly, Hemodynamic mechanisms underlying cerebral aneurysm pathogenesis, Journal of Clinical Neuroscience 18 (2011) 1435–1438.

[4] L. A. Rivera-Rivera, K. M. Johnson, P. A. Turski, O. Wieben, Pressure mapping and hemodynamic assessment of intracranial dural sinuses and dural arteriovenous fistulas with 4D flow MRI, American Journal of Neuroradiology 39 (2018) 485–487.

[5] Y. Li, R. Ahmed, L. A. Rivera-Rivera, J. A. Stadler III, P. Turski, B. Aagaard-Kienitz, Serial quantitative and qualitative measurements of flow in vein of galen malformations using 4-Dimensional flow magnetic resonance imaging (phase contrast vastly undersampled isotropic projection), World neurosurgery 126 (2019) 405–412.

[6] N. Thorin-Trescases, O. de Montgolfier, A. Pinçon, A. Raignault, L. Caland, P. Labbé, E. Thorin, Impact of pulse pressure on cerebrovascular events leading to age-related cognitive decline, American Journal of Physiology-Heart and Circulatory Physiology 314 (2018) H1214–H1224.

[7] O. de Montgolfier, A. Pinçon, P. Pouliot, M.-A. Gillis, J. Bishop, J. G. Sled, L. Villeneuve, G. Ferland, B. I. Lévy, F. Lesage, et al., High systolic blood pressure induces cerebral microvascular endothelial dysfunction, neurovascular unit damage, and cognitive decline in mice, Hypertension 73 (2019) 217–228.

[8] P. D. Hurn, R. J. Traystman, Overview of cerebrovascular hemodynamics, Academic Press: San Diego, CA, 1997.

[9] C. Wu, S. Schnell, P. Vakil, A. Honarmand, S. A. Ansari, J. Carr, M. Markl, S. Prabhakaran, In vivo assessment of the impact of regional intracranial atherosclerotic lesions on brain arterial 3D hemodynamics, American Journal of Neuroradiology 38 (2017) 515–522.

[10] S. C. Smith, T. E. Feldman, J. W. Hirshfeld, A. K. Jacobs, M. J. Kern, S. B. King, D. A. Morrison, W. W. ONeill, H. V. Schaff, P. L. Whitlow, et al., ACC/AHA/SCAI 2005 guideline update for percutaneous coronary intervention: a report of the american college of cardiology/american heart association task force on practice guidelines (ACC/AHA/SCAI writing committee to update the 2001 guidelines for percutaneous coronary intervention), Journal of the American College of Cardiology 47 (2006) e1–e121.

[11] R. A. Nishimura, C. M. Otto, R. O. Bonow, B. A. Carabello, J. P. Erwin, L. A. Fleisher, H. Jneid, M. J. Mack, C. J. McLeod, P. T. OGara, et al., 2017 AHA/ACC focused update of the 2014 AHA/ACC guideline for the management of patients with valvular heart disease: a report of the American College of Cardiology/American Heart Association task force on clinical practice guidelines, Journal of the American College of Cardiology 70 (2017) 252–289.

[12] R. M. Wyman, R. D. Safian, V. Portway, J. J. Skillman, R. G. McKAY, D. S. Baim, Current complications of diagnostic and therapeutic cardiac catheterization, Journal of the American College of Cardiology 12 (1988) 1400–1406.

[13] R. Vitiello, B. W. McCrindle, D. Nykanen, R. M. Freedom, L. N. Benson, Complications associated with pediatric cardiac catheterization, Journal of the American College of Cardiology 32 (1998) 1433–1440.

[14] R. B. Stamm, R. P. Martin, Quantification of pressure gradients across stenotic valves by Doppler ultrasound, Journal of the American College of Cardiology 2 (1983) 707–718.

[15] D. Garcia, J. G. Dumesnil, L.-G. Durand, L. Kadem, P. Pibarot, Discrepancies between catheter and Doppler estimates of valve effective orifice area can be predicted from the pressure recovery phenomenon: practical implications with regard to quantification of aortic stenosis severity, Journal of the American College of Cardiology 41 (2003) 435–442.

[16] T. Feldman, M. Guerrero, Invasive hemodynamic versus Doppler echocardiographic assessment of aortic stenosis severity, Catheter Cardiovasc Interv 87 (2016) 498–499.

[17] D. Marlevi, B. Ruijsink, M. Balmus, D. Dillon-Murphy, D. Fovargue, K. Pushparajah, C. Bertoglio, M. Colarieti-Tosti, M. Larsson, P. Lamata, et al., Estimation of cardiovascular relative pressure using virtual work-energy, Scientific reports 9 (2019) 1375.

[18] A. Vali, M. Aristova, P. Vakil, R. Abdalla, S. Prabhakaran, M. Markl, S. A. Ansari, S. Schnell, Semiautomated analysis of 4D flow MRI to assess the hemodynamic impact of intracranial atherosclerotic disease, Magnetic resonance in medicine 82 (2019) 749–762.

[19] R. Yotti, J. Bermejo, J. C. Antoranz, J. L. Rojo-Álvarez, C. Allue, J. Silva, M. M. Desco, M. Moreno, M. Garcia-Fernandez, Noninvasive assessment of ejection intraventricular pressure gradients, Journal of the American College of Cardiology 43 (2004) 1654–1662.

[20] M. S. Firstenberg, P. M. Vandervoort, N. L. Greenberg, N. G. Smedira, P. M. McCarthy, M. J. Garcia, J. D. Thomas, Noninvasive estimation of transmitral pressure drop across the normal mitral valve in humans: importance of convective and inertial forces during left ventricular filling, Journal of the American College of Cardiology 36 (2000) 1942–1949.

[21] Y.-F. Han, W.-H. Liu, X.-L. Chen, Y.-Y. Xiong, Q. Yin, G.-L. Xu, W.-S. Zhu, R.-L. Zhang, M.-M. Ma, M. Li, et al., Severity assessment of intracranial large artery stenosis by pressure gradient measurements: a feasibility study, Catheterization and Cardiovascular Interventions 88 (2016) 255–261.

[22] Z. Miao, D. S. Liebeskind, W. Lo, L. Liu, Y. Pu, X. Leng, L. Song, X. Xu, B. Jia, F. Gao, et al., Fractional flow assessment for the evaluation of intracranial atherosclerosis: a feasibility study, Interventional Neurology 5 (2016) 65–75.

[23] J. D. Kirsch, M. Mathur, M. H. Johnson, G. Gowthaman, L. M. Scoutt, Advances in transcranial Doppler US: imaging ahead, Radiographics 33 (2013) E1–E14.

[24] M. Markl, A. Frydrychowicz, S. Kozerke, M. Hope, O. Wieben, 4D flow MRI, Journal of Magnetic Resonance Imaging 36 (2012) 1015–1036.

[25] Z. Stankovic, B. D. Allen, J. Garcia, K. B. Jarvis, M. Markl, 4D flow imaging with MRI, Cardiovascular diagnosis and therapy 4 (2014) 173.

[26] A. G. Morgan, M. J. Thrippleton, J. M. Wardlaw, I. Marshall, 4d flow mri for non-invasive measurement of blood flow in the brain: A systematic review, Journal of Cerebral Blood Flow & Metabolism (2020) 0271678X20952014.

[27] S. W. Youn, J. Lee, From 2d to 4d phase-contrast mri in the neurovascular system: Will it be a quantum jump or a fancy decoration?, Journal of Magnetic Resonance Imaging (2020).

[28] J. Liu, L. Koskas, F. Faraji, E. Kao, Y. Wang, H. Haraldsson, S. Kefayati, C. Zhu, S. Ahn, G. Laub, et al., Highly accelerated intracranial 4D flow MRI: evaluation of healthy volunteers and patients with intracranial aneurysms, Magnetic Resonance Materials in Physics, Biology and Medicine 31 (2018) 295–307.

[29] M. Hope, D. Purcell, T. Hope, C. Von Morze, D. Vigneron, M. Alley, W. Dillon, Complete intracranial arterial and venous blood flow evaluation with 4D flow MR imaging, American journal of neuroradiology 30 (2009) 362–366.

[30] M. Aristova, A. Vali, S. A. Ansari, A. Shaibani, T. D. Alden, M. C. Hurley, B. S. Jahromi, M. B. Potts, M. Markl, S. Schnell, Standardized evaluation of cerebral arteriovenous malformations using flow distribution network graphs and dual-venc 4D Flow MRI, Journal of Magnetic Resonance Imaging 50 (2019) 1718–1730.

[31] C. Wu, S. Ansari, A. Honarmand, P. Vakil, M. Hurley, B. Bendok, J. Carr, T. Carroll, M. Markl, Evaluation of 4D vascular flow and tissue perfusion in cerebral arteriovenous malformations: influence of Spetzler-Martin grade, clinical presentation, and AVM risk factors, American Journal of Neuroradiology 36 (2015) 1142–1149.

[32] T. A. Hope, M. D. Hope, D. D. Purcell, C. von Morze, D. B. Vigneron, M. T. Alley, W. P. Dillon, Evaluation of intracranial stenoses and aneurysms with accelerated 4D flow, Magnetic resonance imaging 28 (2010) 41–46.

[33] L. A. Rivera-Rivera, P. Turski, K. M. Johnson, C. Hoffman, S. E. Berman, P. Kilgas, H. A. Rowley, C. M. Carlsson, S. C. Johnson, O. Wieben, 4D flow MRI for intracranial hemodynamics assessment in Alzheimers disease, Journal of Cerebral Blood Flow & Metabolism 36 (2016) 1718–1730.

[34] K. B. Miller, A. J. Howery, L. A. Rivera-Rivera, S. C. Johnson, H. A. Rowley, O. Wieben, J. N. Barnes, Age-related reductions in cerebrovascular reactivity using 4d flow mri, Frontiers in aging neuroscience 11 (2019) 281.

[35] J. Zhang, M. C. Brindise, S. Rothenberger, S. Schnell, M. Markl, D. Saloner, V. L. Rayz, P. P. Vlachos, 4d flow mri pressure estimation using velocity measurement-error-based weighted least-squares, IEEE transactions on medical imaging 39 (2019) 1668–1680.

[36] C. Bertoglio, R. Núñez, F. Galarce, D. Nordsletten, A. Osses, Relative pressure estimation from velocity measurements in blood flows: State-of-the-art and new approaches, International journal for numerical methods in biomedical engineering 34 (2018) e2925.

[37] F. Donati, D. A. Nordsletten, N. P. Smith, P. Lamata, Pressure mapping from flow imaging: enhancing computation of the viscous term through velocity reconstruction in near-wall regions, in: 2014 36th Annual International Conference of the IEEE Engineering in Medicine and Biology Society, IEEE, 2014, pp. 5097–5100.

[38] H. Švihlová, J. Hron, J. Málek, K. Rajagopal, K. Rajagopal, Determination of pressure data from velocity data with a view toward its application in cardiovascular mechanics. part 1. theoretical considerations, International Journal of Engineering Science 105 (2016) 108–127.

[39] M. S. Firstenberg, N. G. Smedira, N. L. Greenberg, D. L. Prior, P. M. McCarthy, M. J. Garcia, J. D. Thomas, Relationship between early diastolic intraventricular pressure gradients, an index of elastic recoil, and improvements in systolic and diastolic function, Circulation 104 (2001) I–330.

[40] D. Marlevi, H. Ha, D. Dillon-Murphy, J. F. Fernandes, D. Fovargue, M. Colarieti-Tosti, M. Larsson, P. Lamata, C. A. Figueroa, T. Ebbers, et al., Non-invasive estimation of relative pressure in turbulent flow using virtual work-energy, Medical Image Analysis 60 (2020) 101627.

[41] D. Marlevi, M. Balmus, A. Hessenthaler, F. Viola, D. Fovargue, A. de Vecchi, P. Lamata, N. S. Burris, F. D. Pagani, J. Engvall, et al., Non-invasive estimation of relative pressure for intracardiac flows using virtual work-energy, Medical Image Analysis (2020) 101948.

[42] J. Schollenberger, C. A. Figueroa, J.-F. Nielsen, L. Hernandez-Garcia, Practical considerations for territorial perfusion mapping in the cerebral circulation using super-selective pseudo-continuous arterial spin labeling, Magnetic resonance in medicine 83 (2020) 492–504.

[43] J. Schollenberger, N. H. Osborne, L. Hernandez-Garcia, C. A. Figueroa, A combined computational fluid dynamics and mri arterial spin labeling modeling strategy to quantify patient-specific cerebral hemodynamics in cerebrovascular occlusive disease, bioRxiv (2021). URL: https://www.biorxiv.org/content/early/2021/01/21/2021.01.21.426887. doi:10.1101/2021.01.21.426887.

[44] C. J. Arthurs, R. Khlebnikov, A. Melville, A. Gomez, D. Dillon-Murphy, F. Cuomo, M. S. Vieira, J. Schollenberger, S. R. Lynch, C. Tossas-Betancourt, et al., CRIMSON: An open-source software framework for cardiovascular integrated modelling and simulation, bioRxiv (2020).

[45] S. Schnell, S. A. Ansari, C. Wu, J. Garcia, I. G. Murphy, O. A. Rahman, A. A. Rahsepar, M. Aristova, J. D. Collins, J. C. Carr, et al., Accelerated dual-venc 4D flow MRI for neurovascular applications, Journal of Magnetic Resonance Imaging 46 (2017) 102–114.

[46] P. G. Walker, G. B. Cranney, M. B. Scheidegger, G. Waseleski, G. M. Pohost, A. P. Yoganathan, Semiautomated method for noise reduction and background phase error correction in MR phase velocity data, Journal of Magnetic Resonance Imaging 3 (1993) 521–530.

[47] M. A. Bernstein, X. J. Zhou, J. A. Polzin, K. F. King, A. Ganin, N. J. Pelc, G. H. Glover, Concomitant gradient terms in phase contrast MR: analysis and correction, Magnetic resonance in medicine 39 (1998) 300–308.

[48] E. Schrauben, A. Wåhlin, K. Ambarki, E. Spaak, J. Malm, O. Wieben, A. Eklund, Fast 4D flow MRI intracranial segmentation and quantification in tortuous arteries, Journal of Magnetic Resonance Imaging 42 (2015) 1458–1464.

[49] S. B. Segletes, W. P. Walters, A note on the application of the extended Bernoulli equation, International journal of impact engineering 27 (2002) 561–576.

[50] C. M. Schirmer, A. M. Malek, Prediction of complex flow patterns in intracranial atherosclerotic disease using computational fluid dynamics, Neurosurgery 61 (2007) 842–852.

[51] X. Leng, F. Scalzo, H. L. Ip, M. Johnson, A. K. Fong, F. S. Fan, X. Chen, Y. O. Soo, Z. Miao, L. Liu, et al., Computational fluid dynamics modeling of symptomatic intracranial atherosclerosis may predict risk of stroke recurrence, PLoS One 9 (2014) e97531.

[52] P. Reymond, F. Perren, F. Lazeyras, N. Stergiopulos, Patient-specific mean pressure drop in the systemic arterial tree, a comparison between 1-D and 3-D models, Journal of biomechanics 45 (2012) 2499–2505.

[53] P. J. Blanco, L. O. Müller, J. D. Spence, Blood pressure gradients in cerebral arteries: a clue to pathogenesis of cerebral small vessel disease, Stroke and vascular neurology 2 (2017) 108–117.

[54] K. L. Ruedinger, R. Medero, A. Roldán-Alzate, Fabrication of low-cost patient-specific vascular models for particle image velocimetry, Cardiovascular engineering and technology 10 (2019) 500–507.

[55] L. Gottwald, J. Töger, K. M. Bloch, E. Peper, B. Coolen, G. Strijkers, P. van Ooij, A. Nederveen, High spatiotemporal resolution 4D flow MRI of intracranial aneurysms at 7T in 10 minutes, American Journal of Neuroradiology 41 (2020) 1201–1208.

[56] E. Ferdian, A. Suinesiaputra, D. J. Dubowitz, D. Zhao, A. Wang, B. Cowan, A. A. Young, 4DFlowNet: Super-resolution 4D Flow MRI using deep learning and computational fluid dynamics, Frontiers in Physics 8 (2020) 138.

[57] O. B. Samuels, G. J. Joseph, M. J. Lynn, H. A. Smith, M. I. Chimowitz, A standardized method for measuring intracranial arterial stenosis, American journal of neuroradiology 21 (2000) 643–646.

[58] Y. Orz, S. Kobayashi, M. Osawa, Y. Tanaka, Aneurysm size: a prognostic factor for rupture, British journal of neurosurgery 11 (1997) 144–149.

[59] D. S. Liebeskind, E. Feldmann, Fractional flow in cerebrovascular disorders, Interventional neurology 1 (2012) 87–99.

Supporting Information Figure S.1: Estimated relative pressures through the right ICA (left) and the right ICA-MCA section (right) in Subject 1. For both sections, results are shown for $dx = 1$ mm and 0.5 mm, with dt = 40 ms in both instances. In each graph, relative pressure estimates are given for RB (green dashed), UB (red dashed), νWERP (blue dashed), and true estimate given by voxelized equivalents of the CFD pressure field generated at the identical spatiotemporal sampling (black solid).

Supporting Information Figure S.2: Linear regression plots, comparing relative pressure estimates obtained at $dx = 1.1$ vs. 0.8 mm using RB, UB, and νWERP, respectively. For reference, νWERP results at $dx = 1.0$ vs. 0.5 mm from the *in-silico* tests (Section 3.1) are shown at the far right.

Supporting Information Figure S.3: Results from both the *in-silico* (spatiotemporal analysis from Section 2.2.2, shown for $dx = 1.0$ and 0.5 mm, cf. Figure 4) and *in-vivo* analysis (linear regression and Bland-Altman plot for $dx = 1.1$ vs. 0.8 mm, cf. Figure 8), utilizing a full Euler UB expression, including $\nabla \mathbf{v}$ in the expression of the advective term.
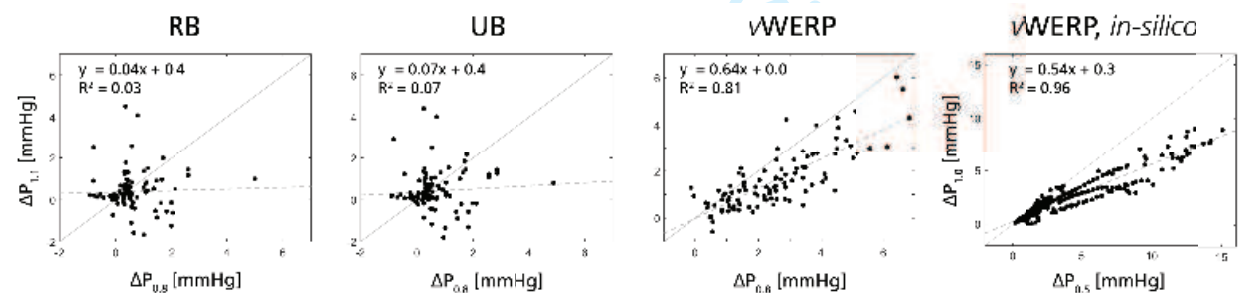
Supporting Information

S.1. Supporting Information - Results

Coupling to the analysis in Section 3.1.1, relative pressure traces for two selected sections (right ICA, and right ICA-MCA) spatiotemporal samplings (dx = 1.0mm, dt = 40 ms, and dx = 0.5mm, dt = 40 ms) are provided in Supporting Information Figure S.1
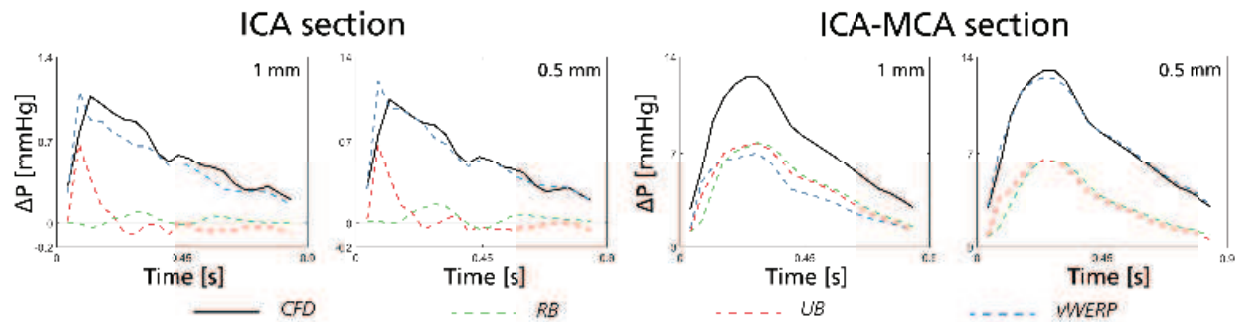
Supporting Information Figure S.1: Estimated relative pressures through the right ICA (left) and the right ICA-MCA section (right) in Subject 1. For both sections, results are shown for $dx = 1$ mm and 0.5 mm, with dt = 40 ms in both instances. In each graph, relative pressure estimates are given for RB (green dashed), UB (red dashed), νWERP (blue dashed), and true estimate given by voxelized equivalents of the CFD pressure field generated at the identical spatiotemporal sampling (black solid).

Furthermore, coupling to the analysis in Section 3.2, linear regression plots for $dx = 1.1$ vs. 0.8 mm are provided for all different evaluated methods, as well as for corresponding *in-silico* data, in Supporting Information Figure S.2.
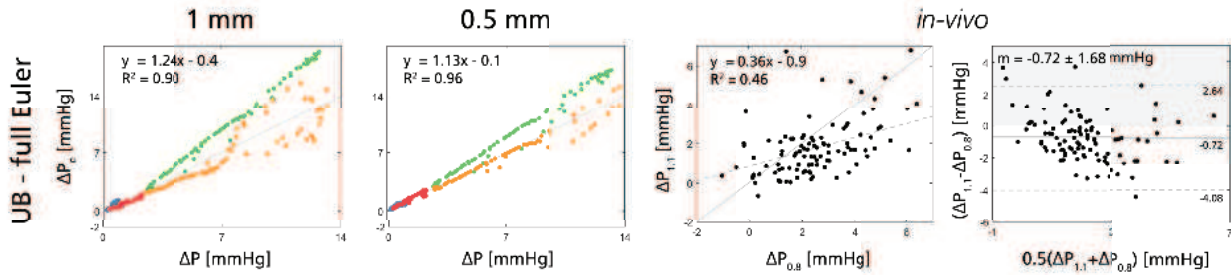

Supporting Information Figure S.2: Linear regression plots, comparing relative pressure estimates obtained at $dx = 1.1$ vs. 0.8 mm using RB, UB, and νWERP, respectively. For reference, νWERP results at $dx = 1.0$ vs. 0.5 mm from the *in-silico* tests (Section 3.1) are shown at the far right.

S.2. Supporting Information - Full Euler formulation and Unsteady Bernoulli

As noted in Sections 2.1 and 4.1.2, UB is based on the assumption that the utilized integration line $\mathbf{p}(s)$ follows a physiological streamline, for which the conversion from Eq. 4 to 5 holds true. In practice, selecting a physiological streamline is however cumbersome. and is often replaced by a user-defined integration line. Importantly, this choice is not
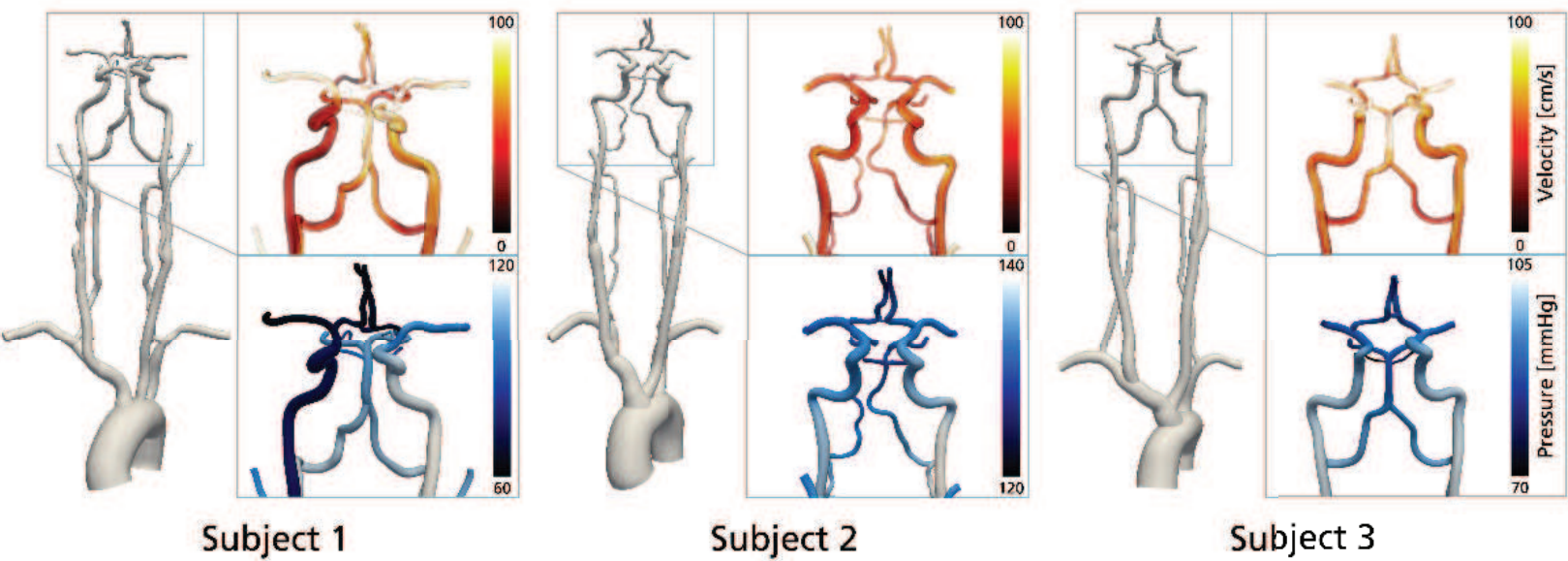
Supporting Information Figure S.3: Results from both the *in-silico* (spatiotemporal analysis from Section 2.2.2, shown for $dx = 1.0$ and 0.5 mm, cf. Figure 4) and *in-vivo* analysis (linear regression and Bland-Altman plot for $dx = 1.1$ vs. 0.8 mm, cf. Figure 8), utilizing a full Euler UB expression, including $\nabla\mathbf{v}$ in the expression of the advective term.
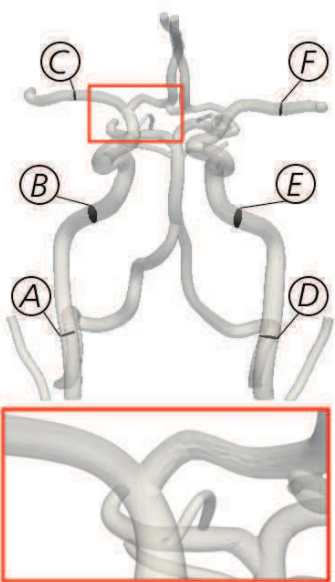
only practical, but works well if assessing predominantly unidirectional flow. If assessing flow with dominant spatial gradients, however, the chosen integration path might no longer validly represent that of a physiological streamline.

To circumvent dependency on utilized integration line, one can instead revert back to the full Euler form given in Eq. 4. Here, the integration path is no longer restricted to that of a physiological streamline, however, derivation requires access to the gradient of the velocity field (as permitted by 4D Flow MRI). Herein, it should be stressed that this formulation represents a non-conventional usage of UB where access to $\nabla\mathbf{v}$ is normally *not* provided (such as when using Doppler echocardiography). Nevertheless, if indeed invoking a full Euler UB expression (Eq. 4), results improve distinctly as shown in Supporting Information Figure S.3, showing exemplifying output from the spatiotemporal analysis (cf. Section 3.1.1) and the *in-vivo* analysis (cf. Section 3.2), respectively. Comparing the standard UB formulation over the spatiotemporal analysis, average d_f decreases to 25.9%, and if focusing on comparably high resolutions ($dt \leq 40$ ms, $dx \leq 0.75$ mm) d_f goes down to 19.8%. Likewise, in the *in-vivo* data correlations between $dx = 1.1$ and 0.8 mm improve slightly, although not to the level observed with νWERP.
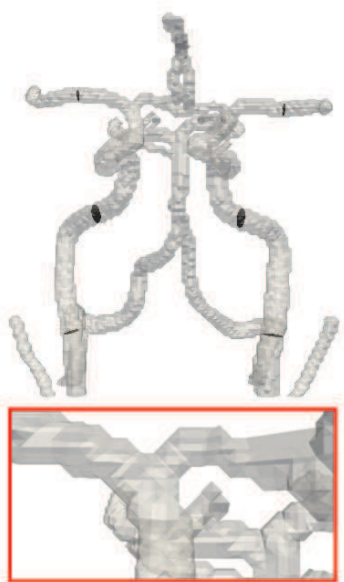
Accurate output can thus in principle be achieved if invoking a full Euler form of the UB. However, it should again be stressed that this does *not* represent the clinical standard use of UB, and the results instead highlight practical obstacles associated with using UB in complex vascular settings.
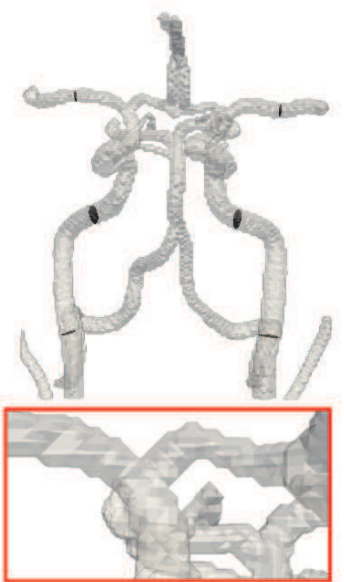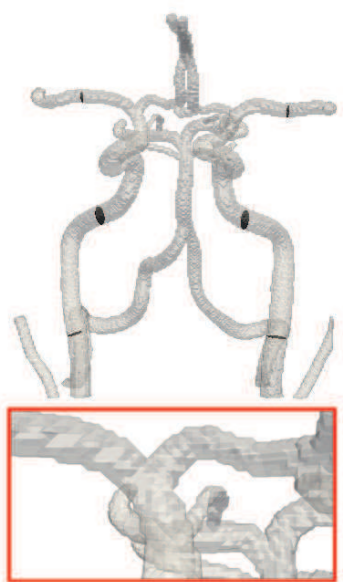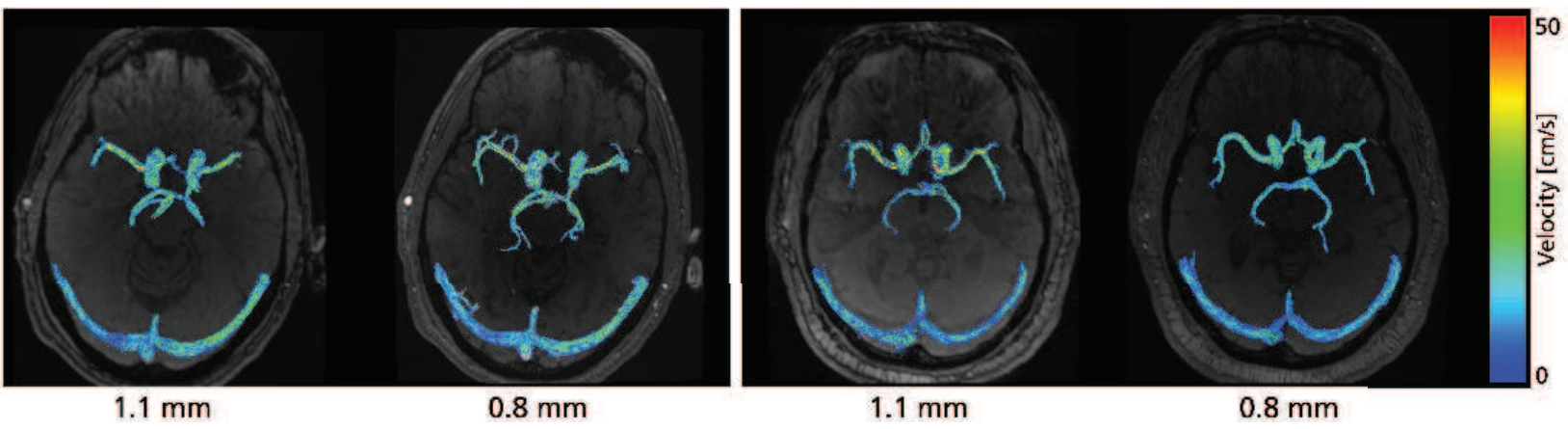
Subject 1   Subject 2   Subject 3

mrm_28928_f1.eps

CFD → 1 mm 0.75 mm 0.5 mm

mrm_28928_f2.eps

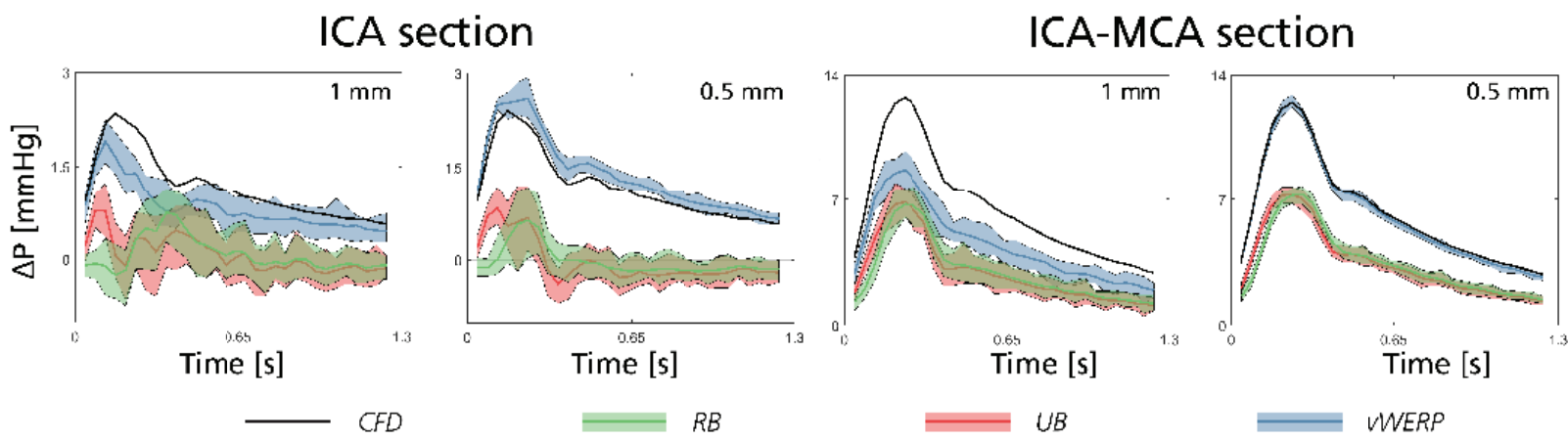1.1 mm   0.8 mm   1.1 mm   0.8 mm

mrm_28928_f3.eps

mrm_28928_f4.eps

ICA section

ΔP [mmHg]

1 mm

0.5 mm

ICA-MCA section

1 mm

0.5 mm

Time [s]

—— CFD   RB   UB   VWERP
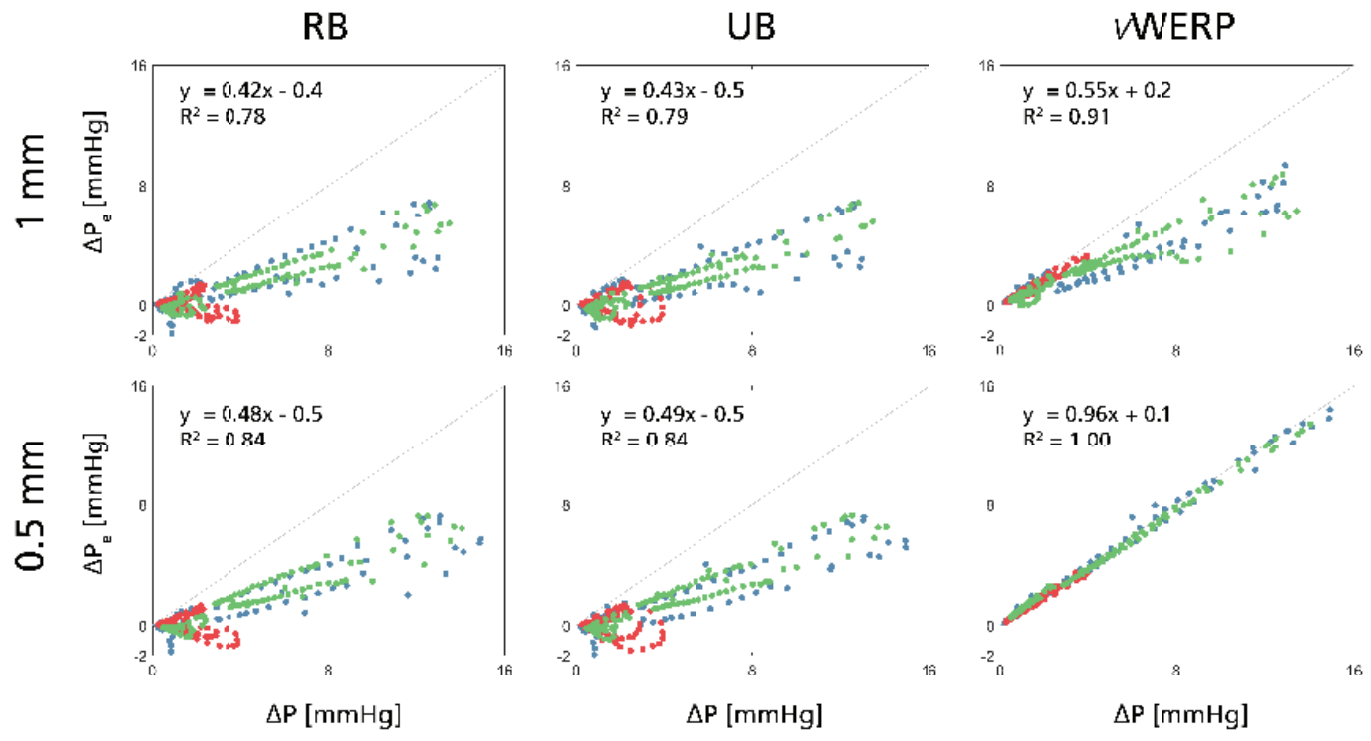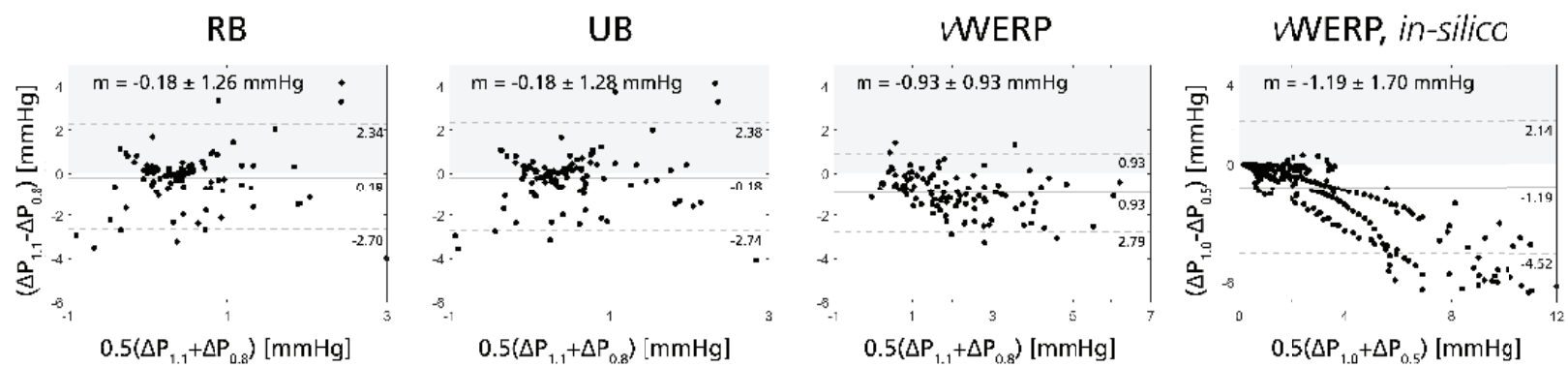
mrm_28928_f5.eps

mrm_28928_f6.eps

mrm_28928_f7.eps

RB — $m = -0.18 \pm 1.26$ mmHg

UB — $m = -0.18 \pm 1.28$ mmHg

vWERP — $m = -0.93 \pm 0.93$ mmHg

vWERP, in-silico — $m = -1.19 \pm 1.70$ mmHg

RB axes: $(\Delta P_{1.1} - \Delta P_{0.8})$ [mmHg] vs $0.5(\Delta P_{1.1} + \Delta P_{0.8})$ [mmHg]; values 2.34, 0.18, -2.70

UB axes: $(\Delta P_{1.1} - \Delta P_{0.8})$ [mmHg] vs $0.5(\Delta P_{1.1} + \Delta P_{0.8})$ [mmHg]; values 2.38, -0.18, -2.74

vWERP axes: $0.5(\Delta P_{1.1} + \Delta P_{0.8})$ [mmHg]; values 0.93, 0.93, 2.79

vWERP, in-silico axes: $(\Delta P_{1.0} - \Delta P_{0.5})$ [mmHg] vs $0.5(\Delta P_{1.0} + \Delta P_{0.5})$ [mmHg]; values 2.14, -1.19, -4.52

mrm_28928_f8.eps